RSC Advances

ROYAL SOCIETY OF CHEMISTRY

www.rsc.org/advances

Graphical Abstract

Blue phase-mixed anatase-rutile TiO_2 heterogeneous junctions composites: surface defect-induced reconstruction by F ion and superior lithium-storage properties†

Hai Wang, Hongxing Yang,* and Lin Lu
Renewable Energy Research Group (RERG), Department of Building Services Engineering, The Hong Kong Polytechnic University, Room: ZN816, Kowloon, Hong Kong, China. Fax: +852-27746146; Tel: +852-27665863; E-mail: bxhxyang@polyu.edu.hk

The surface defect reconstruction of blue phase-mixed anatase-rutile TiO_2 heterogeneous junctions composites plays a crucial role in the enhancement of lithium-ion batteries.

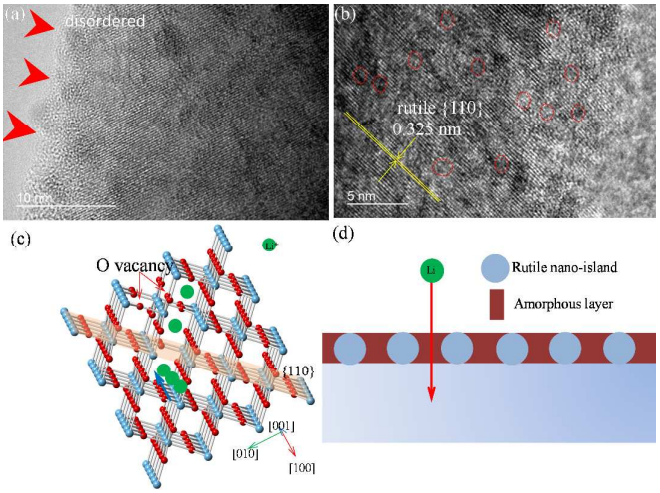

RSC Advances

RSCPublishing

COMMUNICATION

Blue phase-mixed anatase-rutile TiO_2 heterogeneous junctions composites: surface defect-induced reconstruction by F ion and superior lithium-storage properties†

Cite this: DOI: 10.1039/xoxxoooooox

Received ooth January 2012,
Accepted ooth January 2012

DOI: 10.1039/xoxxoooooox

www.rsc.org/

Hai Wang, Hongxing Yang* and Lin Lu

A novel blue phase-mixed anatase-rutile TiO_2 heterogeneous junctions composite, as anode material in lithium ion batteries (LIBs), is built via surface defect induced method. The as-synthesized composites exhibit outstanding rate capability (93 mAh g^{-1} at 20 C), and good cycling stability (7.35% capacity loss after 200 cycles at 10 C).

TiO_2, as anode material in lithium-ion batteries (LIBs) has attracted considerable interest due to their relatively low cost, environmentally friendly nature, and safety.[1-3] However, their intrinsic poor electrical conductivity and poor rate capability practical applications hindered their practical application. To overcome these problems, one promising approach to introduce the conductive Ti^{3+} to enhance the rate capacities of TiO_2-based LIBs.[4, 5] Additionally, the exposed active facet {001} of anatase TiO_2 has also been demonstrated to exhibit superior properties.[2, 6] Therefore, it is expected to obtain satisfactory high capacity and high rate capability using the self-doped Ti^{3+} exposed active facet {001} of anatase TiO_2 as anode materials in LIBs.

Lithium ion diffusion and electron transport often occurs on the surface and interface of electrodes in LIBs during charge-discharge process, which provided many opportunities to obtain the satisfied electrochemical properties, such as amorphous transition metal oxides surface, other heterogeneous oxides.[7-14] Recently, rutile-TiO_2 nanocoating has been proved to be an effective way in improving the electrochemical properties. [12] Inspired by the rutile-TiO_2 nanocoating, for self-doped Ti^{3+} exposed active facets {001} of anatase-TiO_2, how to build a new interface structure different from carbon coating and explore these interface roles are still a great challenge. The aim of this work is to show the importance of the interface role of the self-doped Ti^{3+} exposed active facet {001} of anatase TiO_2, which is of primary importance to understanding the effect of surface/bulk defects on the lithium storage properties.

Herein, we constructed phase-mixed anatase-rutile TiO_2 heterogeneous junctions composites (ART) using surface defect-induced reconstruction with the assistance of F ion. We then investigate their electrochemical behavior by comparing with the ART annealed at 600 ℃ (SART). The results show that the as-synthesized products have integrated all the features of an ideal electrode material: high capacity (the initial discharge capacity: 291 mAh g^{-1} at 0.2 C, long life (7.35% capacity loss after 200 cycles at 10 C), and superior rate capability (93 mA h g^{-1} at a high current density of 20 C). The amorphous layer of ART offers a rather unique electrochemical behaviour, which may be explored in other transition metal oxides.

The ART preparation details are described in the ESI†. As shown in Fig. S1-S3, obviously, the formation of ART is affected by the molar concentration of NaF and HCl solution and reaction time. FESEM images of ART revealed that TiO_2 with exposed facets was closely interconnected, as shown in Fig. 1a and Fig. 1b, and a photo image of blue sample is illustrated in the inset of Fig.1a. The blue shows that the TiO_2 may be doped or other effects factors caused by Ti^{3+}.[15-17] As shown in Fig. 1b, there is a clear boundary located between the adjacent single crystal-like particles. The single ART particle is approximately 500 nm in dimension. Different from previous literature,[18-25] this ART single crystal forms an interconnected network. This interconnected structure not only maintains structural continuity but also results in good electrical contact between the ART particles, which is indispensable for high-performance LIBs.

The TEM and HRTEM were further carried out to reveal the surface and interface of ART and SART, as shown in Fig. 1e-f and Fig. S4. The clear lattice fringes indicate that the obtained ART sample is well-crystallized. Two sets of lattices with an equal lattice fringe spacing of 0.24 nm and 0.325 nm, corresponding to the {004} and {110} planes of anatase and rutile-TiO_2, respectively. Interestingly, TEM images of single ART surface patterned with protruding dots, as shown in Fig. 1d-f. Further HRTEM analysis reveals that these protruding dot is rutile-TiO_2 (Fig. 1f). The good attachment of rutile-TiO_2 to anatase TiO_2 {101} facets can be clearly observed in Fig. 1e. A junction is also indicated in Fig. 1f. Compared to ART, the surface of SART is clear without the presence of protruding dots (Fig. S4).

The XRD patterns of ART and SART are shown in Fig. S5-S6. All the peaks are consistent with the standard pattern anatase JCPDS No. 86-1157 and rutile No. 89-0052 (Fig. S5-6). For ART sample, the phase fraction by weight was determined to ca 89% of anatase and ca 11% of rutile according to the method proposed in the ESI†. The results show that the size of the anatase with exposed {001} and rutile is ca 500 nm and ca 300 nm, respectively. The size of anatase TiO_2 was consistant with the FESEM observation. It is to be

expected that the crystalline size of rutile TiO_2 would become larger after sintering at 600 ℃ according to the Fig. S6b. Of note, the surface morphology of anatase is almost unchanged while the surface defects disappeared strikingly after the heating process (Fig. S4), which allow us for the first time to conduct comparative studies with ART and SART for illustrating the effect of suface and interface on the LIBs performance.

XPS measurements were used to study the chemical states of Ti in the ART and SART. The high-resolution XPS spectrum of Ti 2p (Fig. S7) shows two peaks at binding energies of 458.5 eV (Ti $2p_{3/2}$) and 463.3 eV (Ti $2p_{1/2}$). The Ti 2p peaks are well de-convoluted into four peaks as Ti^{3+} $2p_{3/2}$ (457.37 Ev), Ti^{4+} $2p_{3/2}$ (458.76 eV), Ti^{3+} $2p_{1/2}$ (462.76 eV) and Ti^{4+} $2p_{1/2}$ (464.47 eV).[26, 27] Low temperature electron para-magnetic resonance (EPR) spectra further verify the presence of Ti^{3+} (Fig. S7a-b). Surprisingly, F 1s signal was not detected in ART sample, demonstrating that the surface of anatase may be covered by some unknown coating layer (Fig. S7c). The ART sample gave rise to a very strong EPR signal, while no signal was seen for the SART, (Fig. S7d). The obvious g-values are features of a paramagnetic Ti^{3+} center in a distorted rhombic oxygen ligand field. [28] The EPR data also show that no Ti^{3+} exist on the surface of the SART sample.

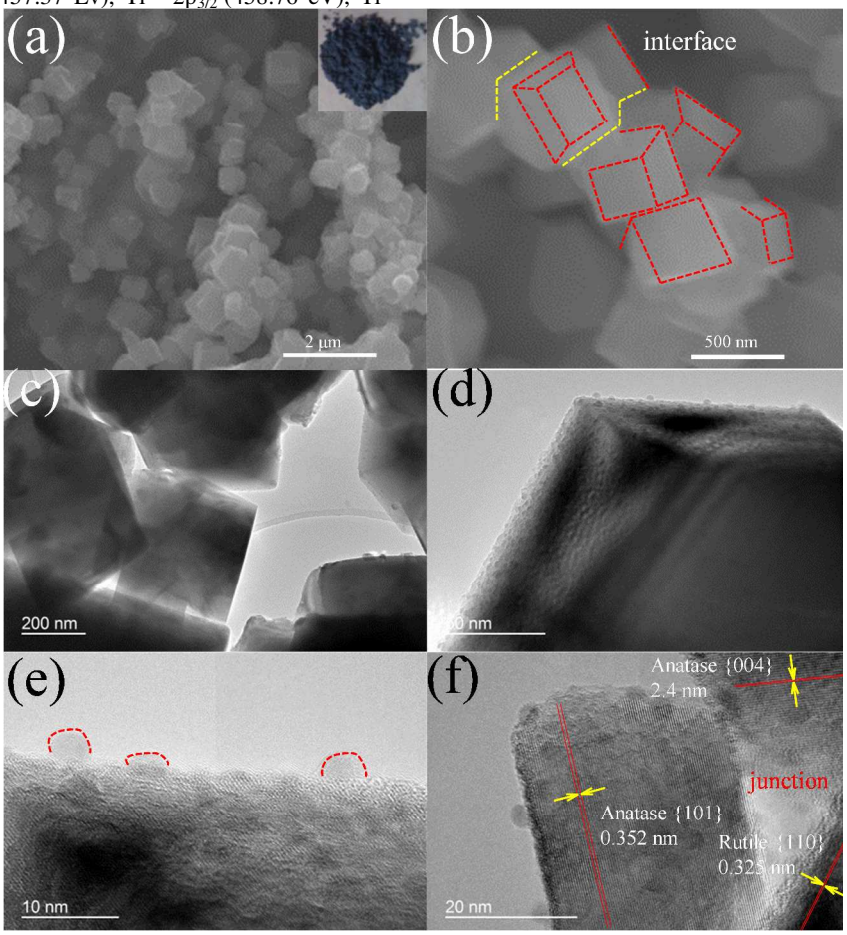

Fig. 1 FESEM image of blue TiO_2 with exposed facets (a)-(b). Inset of (a) is a photo image and a clear dashed yellow line interface in adjacent exposed TiO_2 (b). TEM and HRTEM image of ART sample. HRTEM images of ART (c) and rutile TiO_2 quantum dots are clearly indicated by the dotted lines. The good attachment of rutile TiO_2 to anatase TiO_2 {101} facets can be clearly observed in (e). A junction is also indicated in (f).

Fig. 2a shows the HRTEM image of a representative ART. The HRTEM images of anatase-rutile interface shows rich defects. According to the observed results, we found that the rutile quantum dot was embedded in the expored {101} facets of anatase. In addition, we also find that the rutile-TiO_2 quantum dots were embedded in the amorphous layer (Fig. S8). The SAED image in Fig. 2b also confirmed that the overlay of anatase and rutile along the crystal axis [001]. The simulation of SAED of anatase and rutile was shown in Fig. 2c-d, respectively. As shown in Fig.S8a, the surface of anatase single crystal was covered by an amorphous layer and rutile-TiO_2 quantum dots. Moreover, there are also a large amount of oxygen vacancy defects (Fig. S8b). What is the amorphous layer? The XRD patterns shown in Fig. S5 and S6 are impossible if only rutile-TiO_2 quantum dots appear in the mixture due to the relatively strong diffraction peaks of rutile TiO_2. Based on further TEM observation, we found that the rutile TiO_2 is only an epitaxy layer of anatase TiO_2 {101} facets, although some rutile TiO_2 quantum dots were embedded in the rutile TiO_2 matrix (Fig. S9). Thus, it is concluded that as-obtained blue ART have a core-interface-shell structure; the core is anatase with exposed {001} facets, the shell is rutile-TiO_2, therefore each ART is readily considered as a anatase@interface@rutile core-interface-shell structure with Ti^{3+} localized in the bulk. Additionally, it should be noted that the arrangement of {004} facets of anatase and {110} facets of rutile, and oxygen vacancies of ART not only provide facile transport for lithium-ion insertion and extraction, but also accommodate lithium-ions. Fig. 2e-f shows the illustration of the tunnel structure of the as-prepared ART. Obviously, these open tunnels played a crucial role in facilitating lithium ion insertion and extraction. Moreover, the interconnected structure can also effectively prevent structural collapse and local volumetric variation during the charge-discharge

process, which thus enhances the structural stability and cycling performance.

To demonstrate that the effects of the role of interface on lithium-ion performance, we then compared the lithium storage capacity of the ART, SART crystals as active anode materials at different charge

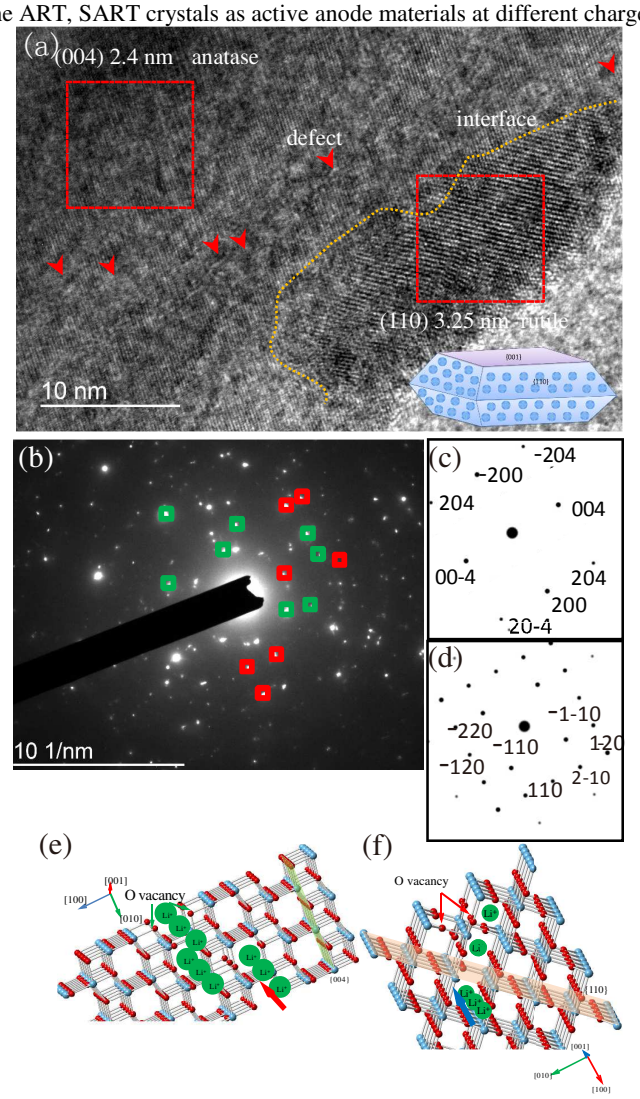

Fig. 2 FESEM image of anatase-rutile interface with rich defects. A schematic image of single anatase-rutile heterogeneous junction (a); (b) a corresponding SAED image in (a); (c)-(d) are the theory SAED of anatase and rutile according to the real SAED image. Illustrations of the crystal structure and Li ion insertion of the anatase (e) and rutile (f) along the [001] projected directions.

-discharge rates from 0.2 to 20 C in the voltage of 1-3 V. At 0.2 C, the ART electrode obtained a first discharge capacity as high as ca 291 mAh g^{-1}, which is much higher than the theoretical value (168 mAh g^{-1}) of TiO_2. What did the extra capacity come from? Zhou group had well documented about the origin of extra storage-lithium performance.[29, 30] For our case, we speculated that one possible reason for extra capacity of ART may be the charge adsorption-desorption on the interface of active materials and electrolytes, i.e., electric double-layer capacitance. The unique surface structure of ART may have an effect on the formation of the SEI thin film during the charge-discharge. Further electrochemical analysis and microstructure observation, such as TEM, after charge-discharge process, will be carried out in the future. On the other hand, the rutile TiO_2 quantum dots will also play an important role, which brought faster lithium ion and electron diffusion inside TiO_2 matrix, and more lithium storage on the surface than in the bulk. It is well-known that most of the nano materials in the form of particles, tubes sheets etc can insert lithium ions up to one Li. $TiO_2+1Li^++1e^- = LiTiO_2$.[31] Therefore, the extra capacity may come from the quantum dots and amorphous layer. The amorphous transition metal oxides had also been demonstrated to play a crucial role in providing extra lithium-storage performance. [7-13]

In contrast, the lithium storage capacity of the ART is significantly improved compared to that of SART sample, corresponding galvanostatic charging-discharging curves of each sample are given in Fig. 3a-b. Moreover, the ART electrode possesses better cyclic stability than SART (Fig. 3c). After 200 cycles the discharge capacity of the ART was 101 mAh g^{-1} at 5 C with only 20% capacity loss, while for SART, the corresponding values were 63 mAh g^{-1} and 19%. Specially, the specific discharge capacity of the ART at 20 C is 110 mAh g^{-1} while the corresponding capacity of the SART is only 79 mAh g^{-1}, indicating the superior lithium storage properties of ART.

The rate performance of pristine ART and SART at various charge-discharge rates were compared in Fig. 3d. At 0.2 C rate, the SART exhibits high initial discharge capacity (286 mAh g^{-1}), followed by a sharp capacity decay with the increase of current rate. ART, however, exhibited much higher lithium storage capacity and much better rate capability than SART. For example, at 10 C and 20 C, the discharge capacity of ART was more than that of SART. Although the stability of two electrodes indicates similar stability, the capacities decrease with increasing current density rate, the ART still shows a high capacity with excellent capacity retention even at the higher rate of 10 C (Fig.S10). Moreover, the difference value of the capacities between the ART and SART electrodes become larger when the current rate increases gradually. The results show that the interface effectively enhanced lithium-ion storage capacity and improved storage kinetics, especially at high rates. It should be noted that the ART still delivers superior high rate lithium storage capacity, though the specific surface area of the ART sample is ca 10.11 m^2 g^{-1}, which is lower than that of SART (Fig. S11 and Table S1). The thin rutile TiO_2 layer on the surface protects SEI thin film from being formed by synergistic effect of amorphous layer, making it beneficial for the LIBs applications. Thus, this unusual phase junctions composites could be expected to exhibit greatly enhanced stability and during the charge-discharge process.

A comparison curve of the cyclic voltammogram (CV) for SART and ART is shown in Fig. 3e. Obviously, the peak shape of ART was sharper and intense, and the gap between redox peaks was smaller than that of SART, indicating that the former had lower overall resistance and greater efficiency of the redox reaction. This low ionic and electronic resistance collaborated well with the electrochemical impedance spectroscopy results presented in Fig. 4f. In Table S2, the ART electrode shows a much lower charge-transfer resistance than that of the SART electrode (72.3 vs 138.4 Ω) on the basis of the modified Randles equivalent circuit given in the inset of Fig. 4f. The origin of the much lowered resistance may be the modified electronic structure as a result of self-doped Ti^{3+} and amorphous layer.

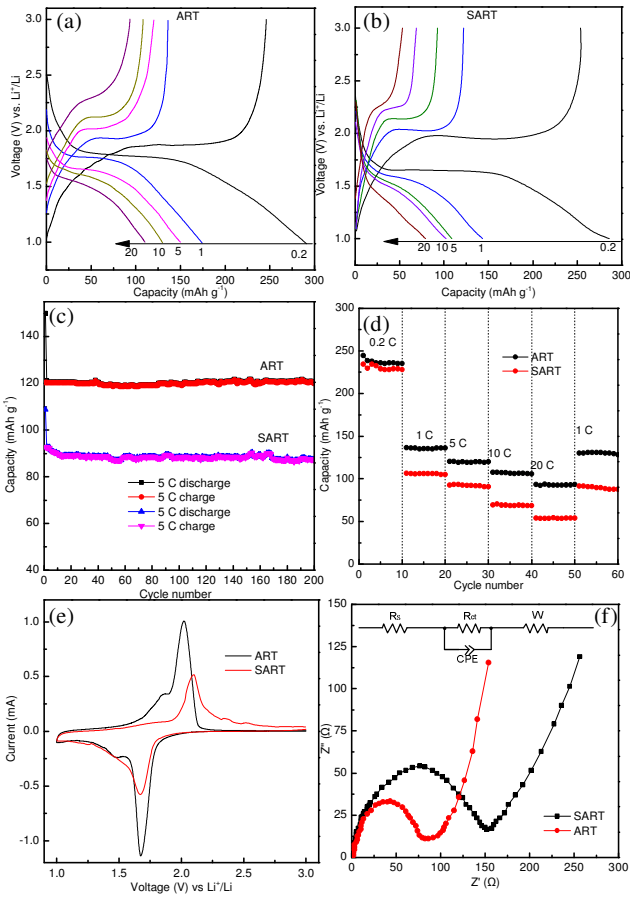

Fig. 3 Comparison of Electrochemical properties of ART and SART: the charge-discharge curves of (a) ART and (b) SART; c) Specific discharge capacities at various C rates; (d) Cycling performances at the rate of 5 C; (e) Cyclic voltammograms; f) Nyquist plots.

How did the heterogeneous-junction structure of the ART especially for the high-rate performance? According to our experimental results, superior electrochemical properties synergistically attributed to the interface structure: amorphous layer and rutile quantum dots, and conductive Ti^{3+}. In our work, the relationship between the heterogeneous-junction structure and high-rate performance has not been reasonably explained. On one hand, we focus the interconnected structure of phase-mixture anatase-rutile TiO_2 heterogeneous junctions may be beneficial for the structure stability, which provides an important platform for high-performance lithium-ion batteries during the high-rate charge-discharge process. To really address this issue, a reasonable materials design and comparison experiments should be carried out. For example, the comparison of electrochemical performance for the three samples: anatase, rutile, the anatase-rutile TiO_2 heterogeneous junctions composites. However, it is considerable difficult to design such a perfect structure since the lithium-ion batteries performance is obviously affected by some other structural parameters of anode materials, such as specific surface area, particles size, pore structure, and so on. It is very difficult to guarantee that a condition was fixed while maintaining the other conditions remain unchanged. Therefore, we only make a comparison of surface structure so as to illustrate a conceptual problem: the surfaces structure reconstruction will have a significant impact on high-performance lithium-ion battery.

Whether this heterogeneous-junction structure will affect the performance of lithium-ion batteries have a causal relationship, it is a good scientific issue. The issue would be explored in the future.

In conclusion, we have demonstrated that the lithium storage properties of TiO_2 with exposed {001} facets electrodes are directly related to the surface and interface structure of electrodes. More interestingly, it is found that the superior electrochemical properties should be synergistically attributed to their interface structure: amorphous layer and rutile-TiO_2 quantum dots, and conductive Ti^{3+}. This works show that designing and building surface structure of electrodes will bring new opportunities for the development of high-performance LIBs.

This work was financially supported by PolyU's Postdoctoral Dean Reserve Project (1-ZV9F) and Guangxi Natural Science Foundation (No.2014GXNSFAA118349).

Notes and references

Renewable Energy Research Group (RERG), Department of Building Services Engineering, The Hong Kong Polytechnic University, Room: ZN816, Kowloon, Hong Kong, China. Fax: +852-27746146; Tel: +852-27665863; E-mail: bxhxyang@polyu.edu.hk.

† Electronic Supplementary Information (ESI) available: Experimental details. See DOI: 10.1039/c000000x/.

Angew. Chem. Int. Ed., 2012, **51**, 2164-2167.
2 J. S. Chen, Y. L. Tan, C. M. Li, Y. L. Cheah, D. Y. Luan, S. Madhavi, F. Y. C. Boey, L. A. Archer and X. W. Lou, *J. Am. Chem. Soc.*, 2010, **132**, 6124-6130.
3 S. H. Liu, H. P. Jia, L. Han, J. L. Wang, P. F. Gao, D. D. Xu, J. Yang and S.
N. Che, *Adv. Mater.*, 2012, **24**, 3201-3204.
4 C. L. Olson, J. Nelson and M. S. Islam, *J Phys Chem B*, 2006, **110**, 9995-10001.
5 S. T. Myung, M. Kikuchi, C. S. Yoon, H. Yashiro, S. J. Kim, Y. K. Sun and B. Scrosati, *Energ. Environ. Sci.*, 2013, **6**, 2609-2614.
6 C. H. Sun, X. H. Yang, J. S. Chen, Z. Li, X. W. Lou, C. Z. Li, S. C. Smith, G. Q. Lu and H. G. Yang, *Chem. Commun.*, 2010, **46**, 6129-6131.
7 E. Peled, C. Menachem, D. BarTow and A. Melman, *J Electrochem Soc*, 1996, **143**, L4-L7.
8 S. T. Myung, K. Izumi, S. Komaba, Y. K. Sun, H. Yashiro and N. Kumagai,
Chem Mater, 2005, **17**, 3695-3704.
9 C. Hin, *Adv Funct Mater*, 2011, **21**, 2477-2487.
10 D. Takamatsu, Y. Koyama, Y. Orikasa, S. Mori, T. Nakatsutsumi, T. Hirano, H. Tanida, H. Arai, Y. Uchimoto and Z. Ogumi, *Angew. Chem. Int. Ed.*,, 2012, **51**, 11597-11601.
11 J. B. Goodenough and Y. Kim, *Chem. Mater.*, 2010, **22**, 587-603.
12 Y. Q. Wang, L. Guo, Y. G. Guo, H. Li, X. Q. He, S. Tsukimoto, Y. Ikuhara and L. J. Wan, *J. Am. Chem. Soc.*, 2012, **134**, 7874-7879.
13 J. Lu, Q. Peng, W. Y. Wang, C. Y. Nan, L. H. Li and Y. D. Li, *J. Am. Chem. Soc.*, 2013, **135**, 1649-1652.
14 Y. Z. Jiang, D. Zhang, Y. Li, T. Z. Yuan, N. Bahlawane, C. Liang, W. P. Sun, Y. H. Lu and M. Yan, *Nano Energy*, 2014, **4**, 23-30.
15 F. Zuo, L. Wang, T. Wu, Z. Y. Zhang, D. Borchardt and P. Y. Feng, *J. Am. Chem. Soc.*, 2010, **132**, 11856-11857.
16 A. Teleki and S. E. Pratsinis, *Phys. Chem. Chem. Phys.*, 2009, **11**, 3742-3747.
17 G. Liu, H. G. Yang, X. W. Wang, L. N. Cheng, H. F. Lu, L. Z. Wang, G. Q. Lu and H. M. Cheng, *J. Phys. Chem. C.*, 2009, **113**, 21784-21788.
18 H. M. Zhang, X. L. Liu, Y. Wang, P. R. Liu, W. P. Cai, G. S. Zhu, H. G. Yang and H. J. Zhao, J. Mater. Chem. A., 2013, **1**, 2646-2652.
19 X. Y. Ma, Z. G. Chen, S. B. Hartono, H. B. Jiang, J. Zou, S. Z. Qiao and H. G. Yang, *Chem. Commun.*, 2010, **46**, 6608-6610.
20 L. Wang, L. Zang, J. C. Zhao and C. Y. Wang, *Chem. Commun.*, 2012, **48**,
11736-11738.
21 H. M. Zhang, Y. H. Han, X. L. Liu, P. R. Liu, H. Yu, S. Q. Zhang, X. D. Yao and H. J. Zhao, *Chem. Commun.*, 2010, **46**, 8395-8397.
22 H. Yu, B. Z. Tian and J. L. Zhang, *Chem.Eur. J.*, 2011, **17**, 5499-5502.
23 J. J. Fan, W. Q. Cai and J. G. Yu, *Chem.Asian J.*, 2011, **6**, 2481-2490.

24 W. Q. Fang, X. H. Yang, H. J. Zhu, Z. Li, H. J. Zhao, X. D. Yao and H. G. Yang, *J. Mater. Chem.*, 2012, **22**, 22082-22089.
25 S. W. Liu, J. G. Yu and M. Jaroniec, *J. Am. Chem. Soc.*, 2010, **132**, 11914-11916.
26 A. Sandell, M. P. Andersson, M. K. J. Johansson, P. G. Karlsson, Y. Alfredsson, J. Schnadt, H. Siegbahn and P. Uvdal, *Surf. Sci.*, 2003, **530**, 63-70.
27 J. Pouilleau, D. Devilliers, H. Groult and P. Marcus, *J. Mater. Sci.*, 1997, **32**, 5645-5651.
28 V. M. Khomenko, K. Langer, H. Rager and A. Fett, *Phys. Chem. Miner.*, 1998, **25**, 338-346.
29 L. W. Su, Y. R. Zhong and Z. Zhou, *J. Mater. Chem. A.*, 2013, **1**, 15158-15166.
30 M. M. Zhen, L. W. Su, Z. H. Yuan, L. Liu and Z. Zhou, *RSC Adv.*, 2013, **3**, 13696-13701.
31 M. V. Reddy, X. W. V. Teoh, T. B. Nguyen, Y. Y. M. Lim and B. V. R. Chowdari, *J. Electrochem. Soc.*, 2012, **159**, A762-A769.